

MEASUREMENT OF RICE MOISTURE CONTENT BASED ON QUANTITATIVE ANALYSIS FROM RADIO TOMOGRAPHY IMAGES

Nurul Amira Mohd Ramli^a, Mohd Hafiz Fazalul Rahiman^{a,b,*}, Ruzairi Abdul Rahim^c, Latifah Munirah Kamarudin^{b,d}, Latifah Mohamed^{a,b}, Ammar Zakaria^{a,b}, Mohammed Saeed Moqbel Abdullah^a

Article history

Received
27 August 2023
Received in revised form
12 October 2023
Accepted
26 November 2023
Published Online
20 April 2024

^aFaculty of Electrical Engineering and Technology, Universiti Malaysia Perlis, Pauh Putra Campus, 02600, Arau, Perlis, Malaysia

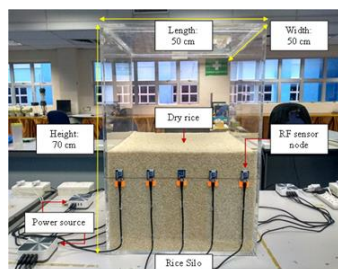
^bCentre of Excellence for Advanced Sensor Technology, Universiti Malaysia Perlis, 02600, Arau, Perlis, Malaysia

^cFaculty of Electrical and Electronic Engineering, Universiti Tun Hussein Onn Malaysia, 86400 Parit Raja, Batu Pahat Johor, Malaysia

^dFaculty of Electronic Engineering and Technology, Universiti Malaysia Perlis, Pauh Putra Campus, 02600, Arau, Perlis, Malaysia

*Corresponding author
hafiz@unimap.edu.my

Graphical abstract



Abstract

Inefficient storage of paddy and rice grains can lead to grain deterioration, resulting in post-harvest losses ranging from 10% to 30%. The quality of grains cannot be improved throughout the storage period. Therefore, following the mechanisation of agricultural industries, air dryers have been developed to control the crops' moisture level by blowing ambient or heated air into the silo to improve the aeration and allow the grains to be preserved with minimal loss of quality until the appropriate time for managing and marketing processes. However, the conventional sampling method used to measure the moisture level is inefficient because it is very localised and only represents part of the moisture distribution inside the bulk grains. Additionally, incorporating advanced technologies can be a significant cost limitation for small-scale industries. Thus, to address the issue, this research study developed a radio tomographic imaging (RTI) system in a silo-scale prototype using 20 sensor nodes operating at 2.4 GHz to localise and monitor the moisture level constructively. The RTI system reconstructs the cross-sectional images across the rice silo by measuring radio frequency attenuation, in terms of received signal strength (RSS) quality, caused by the rice moisture phantoms within the wireless sensor network (WSN) area. A total of five phantoms' profiles having a percentage of moisture content (MC) of 15%, 20% and 25% were reconstructed using four image reconstruction algorithms, Linear Back Projection (LBP), Filtered Back Projection (FBP), Newton's One-step Error Reconstruction (NOSER) and Tikhonov Regularisation. Then, an image quality assessment, Mean Structural Similarity Index (MSSIM), was utilised to evaluate the performance of the reconstructed images. Lastly, a numerical method based on the first-order linear regression model was introduced as a preliminary approach toward the method's establishment. In summary, the experimental results demonstrated average image quality scores for all MC levels (15%, 20% and 25%), where the range scores are 0.2776 – 0.4755. Based on the numerical analysis, the results support the possibility of engaging the proposed technique to monitor the moisture level inside a rice silo with the highest and lowest correlation coefficients of 0.7218 and 0.5442, respectively.

Keywords: Image reconstruction, radio tomography, received signal strength, grain moisture sensing, moisture measurement

Abstrak

Proses penyimpanan bijirin padi dan beras padi yang tidak cekap boleh menyebabkan kemerosotan nilai bijirin, sekaligus mengakibatkan kerugian selepas tuaian antara 10% hingga 30%. Kualiti bijirin tidak boleh dipertingkatkan sepanjang tempoh penyimpanan. Oleh itu, berikutan mekanisasi industri pertanian, penering udara telah dibangunkan untuk mengawal tahap kelembapan bijirin dengan mensalurkan udara sekeliling atau yang dipanaskan ke dalam silo untuk meningkatkan pengudaraan dan membolehkan bijirin dipelihara daripada kemerosotan kualiti sehingga masa yang sesuai untuk pengurusan seterusnya atau proses pemasaran. Walau bagaimanapun, kaedah persampelan konvensional yang telah digunakan untuk mengukur tahap kelembapan mungkin tidak cekap kerana ia sangat setempat dan tidak mewakili keseluruhan taburan kelembapan secara pukal di dalam silo. Selain itu, menggabungkan teknologi canggih boleh menjadi faktor kos yang ketara tinggi untuk industri berskala kecil. Oleh itu, untuk menangani isu tersebut, kajian penyelidikan ini membangunkan sistem pengimejan tomografi radio (RTI) di dalam silo berskala prototaip menggunakan 20 nod penerima yang beroperasi pada frekuensi 2.4 GHz untuk menyetempat dan mengukur tahap kelembapan dengan lebih baik. Sistem RTI ini membina semula imej keratan rentas merentasi silo beras dengan mengukur pengurangan frekuensi radio, dari segi kualiti kekuatan isyarat (RSS) yang diterima, yang disebabkan oleh profil kelembapan beras di dalam kawasan rangkaian penerima tanpa wayar (WSN). Sebanyak lima profil beras yang mempunyai peratusan kandungan kelembapan (MC) sebanyak 15%, 20% dan 25% telah dibina semula menggunakan empat algoritma pembinaan semula imej, Unjuran Belakang Lurus (LBP), Unjuran Belakang Ditapis (FBP), Pembinaan Semula Ralat Satu Langkah Newton (NOSER) dan Regularisasi Tikhonov. Kemudian, penilaian kualiti imej, Mean Structural Similarity Index (MSSIM), digunakan untuk menilai prestasi imej yang dibina semula. Akhir sekali, kaedah berangka berdasarkan model regresi lurus telah diperkenalkan sebagai pendekatan awal ke arah pembentukan kaedah yang disarankan. Secara ringkasnya, keputusan eksperimen menunjukkan purata skor kualiti imej untuk kesemua peringkat MC (15%, 20% dan 25%), di mana skor julat adalah 0.2776 – 0.4755. Berdasarkan analisis berangka, keputusannya menyokong kemungkinan menggunakan teknik yang dicadangkan untuk memantau tahap kelembapan di dalam silo beras dengan pekali korelasi tertinggi dan terendah sebanyak 0.7218 dan 0.5442, masing-masing.

Kata kunci: Pembinaan imej, tomografi radio, kualiti kekuatan isyarat, pengesanan kelembapan bijirin, pengukuran kelembapan

© 2024 Penerbit UTM Press. All rights reserved

1.0 INTRODUCTION

Generally, the quality of rice grains is defined by the attributes of their physicochemical characteristics [1, 2]. The composition of chemical properties, which leads to their nutritional value, comprises variations of amylose content, starches, and gelatinisation temperature. Meanwhile, the physical qualities that determine the market value include the whiteness, uniformity of grains dimension, head rice and the colour of the grains. According to the review by [2], the presence of moisture content (MC) appears to be a critical factor that tends to alter these attributes. MC is referred to as the wet basis, meaning the total weight of the grain, including the water (MC w.b.), expressed in percentage.

As per the analysis conducted [3, 4, 5], to sustain the quality of paddy and rice grains and allow long-term storage, they must be dried down to 12 – 14% MC, depending on the local weather conditions, storage durations and types of storage. Grains with a higher percentage of MC tend to be frail, which may be pulverised and encourage the growth of fungal attack, whereas if the percentage of MC is too low,

the grains become brittle and are exposed to a higher rate of breakage [5, 6, 7].

Over the past decades, [8] has presented the dielectric properties of grains and seeds as a function of the applied frequency, their percentage of moisture content, as well as the temperature and density of these materials. They are practically expressed as the complex permittivity relative to free space, $\epsilon_r = \epsilon' - j\epsilon''$ [9]. The real part, ϵ' is the dielectric constant associated with the grain's ability to store the applied electrical energy, while the imaginary part, ϵ'' is known as the dielectric loss factor, which represents the dissipation of applied electrical energy in the form of heat. Their properties, therefore, are significant for the agricultural industry, especially in moisture level-sensing applications [10]. For particular application of moisture sensing, [11] has also discussed that electromagnetic radiation greatly influences the dielectric materials due to their natural polarisation of water molecules.

The recorded quantitative data by [12] has summarised the correlation of dielectric properties of various rice cultivars with frequencies ranging from 50 Hz to 12 GHz and the percentage of MC ranging from 11 – 21%. The authors concluded that the dielectric

constant consistently increased with the percentage of MC over a higher to lower frequency range. In contrast, the behaviour of the loss factor is less predictable where there were linear increases and decreases in the data with the percentage of MC at some different ranges of frequencies. Lastly, they also found that the conductivity of all kinds of rice is directly proportional to the frequency values. This characteristic has evolved into promising commercial techniques that could improve the efficiency of moisture sensing and explore practical moisture sensing employment in the storage monitoring process.

Ever since the discovery of grains MC and their associated dielectric properties, an exciting evolution of moisture sensing techniques has been established [13]. Some of these current techniques have offered a convenient, low cost and provide rapid measurement, which is beneficial for the moisture sensing application. Nonetheless, from a specific point of view, the most common disadvantage among them is the employment of the sampling method, where only a few grams of grain sample are treated, making them apply a destructive process and eventually inefficient in monitoring moisture distribution within bulk storage.

Therefore, this study proposed a radio tomographic imaging (RTI) system to improve the performance of moisture distribution sensing in rice silos, comparatively offering a distinctive approach to determine the properties of rice MC without altering or tearing down the features of the grains. The proposed method focuses on tomogram analysis produced by developing an RTI system for monitoring the moisture distribution inside an experimental lab-scaled rice silo setup. The remarkable approach of this technique is that it allows repeatable measurements on the same material over a duration of time, which in future could be applied to monitor several material properties corresponding with the control system as desired.

2.0 METHODOLOGY

Previously, the application of process tomography for moisture assessment has customised numerous hard-field and soft-field sensory systems. Some of the tomography sensors designed for different kinds of moisture detection and monitoring systems are, for example, studies involving cementitious materials [14], quantifying a 3D geometrical cracking behaviour in solid clayey soil [15], determination of local moisture content for wood in real-time measurement [16], study to assess the moisture distribution in a damp historical building [17], investigating the moisture patterns under the homogeneous soil during rainfall incidents [18], and spotting wet wood presence in the silver fir trees [19]. To summarise, the deployed sensor structure serves as the core input to the system, which is built primarily based on the suitability of the surrounding, the nature of the object of interest and the resolution quality of the information required by the user [20, 21].

Figure 1 illustrates the block diagram of a process tomography system [22, 23]. The system's composition can be separated into three basic structures: the sensory system, the data interface part, and the image reconstruction system for producing the tomogram. The sensing facility consists of sensors, measurement circuits and signal conditioning circuits to measure and transmit data from the sensing area to the data acquisition system. Finally, in the image reconstruction part, the theoretical sensor output is firstly interpreted by solving the forward problem, and then the tomogram is built by solving the inverse problem using the image reconstruction algorithm.

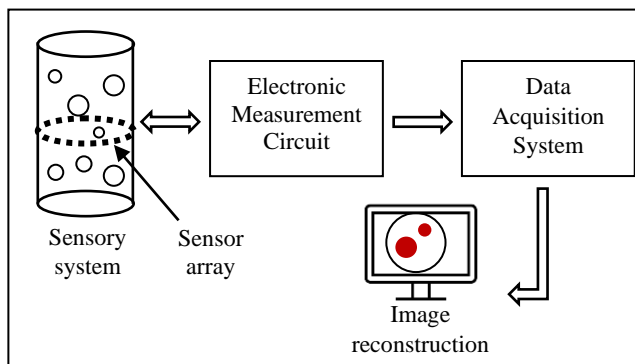


Figure 1 Block diagram of a process tomography system

This section aims to explain the research methodology, consisting of three subsections. The first subsection starts with explanations of the hardware design involved in the RTI system. The next subsection discusses the forward and inverse problems related to the image reconstruction technique. Lastly, an image enhancement analysis is described to improve the quality of the reconstructed images.

2.1 Hardware Design

The concept of the RTI technique was initially proposed by [24]. This technology enables the monitoring and locating static or moving targeted objects using image reconstruction based on changes in the received signal strength (RSS) between each stationary sensor link within the wireless sensor network (WSN) area. The wireless network is termed an "RF sensor network" because the network itself is the sensor that measures the signals attenuation of each transmission link between the RF sensor nodes. It is understood that when an object obstructs the transmission links, the RSS quality of the associated links will experience a significant loss, whereas unblocked links remain unaffected. Hence, the RTI system monitors and localises the targeted object by reconstructing the RSS attenuation map across the network area.

Figure 2 shows the hardware measurement setup for the RTI system. In this preliminary investigation, the rice silo is conceptualised to investigate the capability of the RTI system to image the moisture distribution

inside the rice silo. As the propagation mechanism of electromagnetic waves involves wave scattering, diffraction, and reflection, the silo configuration is carefully determined to facilitate electromagnetic wave interference within the silo [25, 26]. It takes the formation of a 50 x 50 cm square base with a height of 70 cm, constructed from a robust acrylic plate with a thickness of 1 cm.

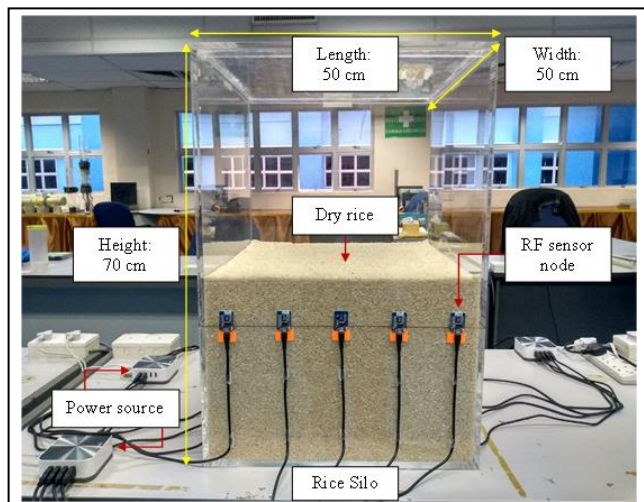


Figure 2 RTI measurement system set-up

The rice silo is also equipped with 20 RF sensor nodes evenly distributed around the perimeter of the square silo, operating at a frequency of 2.4 GHz, to take advantage of the low-cost, over-the-shelf Wi-Fi sensors and the standard ISM band of the WSN. In this study, the number of RF sensor nodes is specifically considered to enhance the quality of the reconstructed images because a greater number of projection links intersect at specific points, leading to better imaging results [27, 28].

2.1.1 Setting of Moisture Content Phantom

Ideally, the evaluation of the RTI system should involve the build-up of moisture spots that are naturally distributed across the silo. However, due to the high cost of the rice grains, this study avoided intentionally inducing uncontrolled spoilage. Thus, the experiment utilized cylindrical containers to house the rice phantoms throughout the entire experiment. Figure 3 shows the two sizes of cylindrical containers to represent the small and big rice moisture phantoms, each holding a total volume of 2.1 L and 5.6 L, respectively. The heights of the containers may differ, but both containers are filled with rice moisture consistently at a height of approximately 22 cm. The thickness of both containers, which is 1 mm, can be considered negligible compared to the wavelength of the radiating frequency at 2.4 GHz, which is 124.91 mm [29].

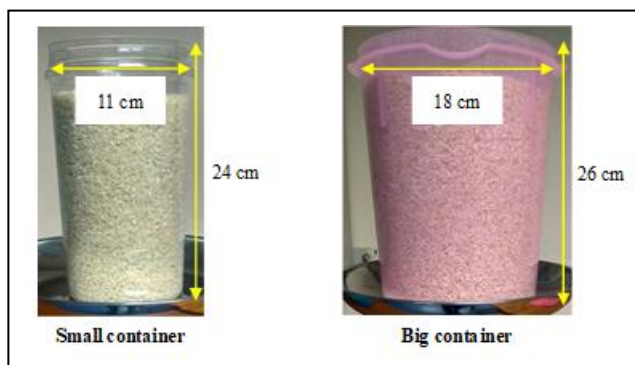


Figure 3 Details of the physical containers representing the rice moisture phantoms

Several sets of known rice moisture phantoms have been used to test and validate the performance of the RTI system. The dry rice stored in the silo usually has an MC of 12 – 14%, as it is the standard percentage of rice MC after the drying process, subsequently for marketing purposes [3, 30]. For the rice moisture phantoms, the MC is set incrementally by 5% each time it is increased, starting at 15%, 20%, and finally 25%. The highest MC percentage of 25% exemplifies the worst condition for rice moisture phantom since the paddy grains are typically harvested when the percentage of MC is between 24% and 26% [3, 30].

The percentage of MC is adjusted to the desired set based on the moistening method used in the previous study [31]. A predetermined amount of water, Q in kg, is calculated by Equation (1).

$$Q = \frac{W_i(M_d - M_i)}{(100 - M_d)} \quad (1)$$

Where W_i is the initial mass of the rice grains (kg), M_i is the initial percentage of the rice MC (% wet basis) and M_d is the desired percentage of the rice phantom (% wet basis).

The flow process performed for sample preparation of rice moisture phantoms is as in references [31, 32]. Firstly, the initial percentage of rice MC is measured using a commercial Grain Moisture Meter (MC-7828G). The recorded initial MC of rice for all the experimental studies ranged from 11.30% to 13.80%. Next, approximately 1.5 kg and 3.7 kg of the rice are weighed using a weighing scale and loaded into the small and big containers, respectively. The determined amount of water, Q is then added to the sample as per the desired percentage of MC. Finally, the container is left for the water to be entirely absorbed until no excess water can be drained. The container was shaken regularly throughout the moisture setting to ensure the rice moisture sample was evenly moistened. The experimental study repeats the flow process for all rice moisture phantoms studied.

Figure 4 illustrates the five rice moisture phantoms, Phantom A, B, C, D and E, involving single and multiple positions considered in this experimental study.

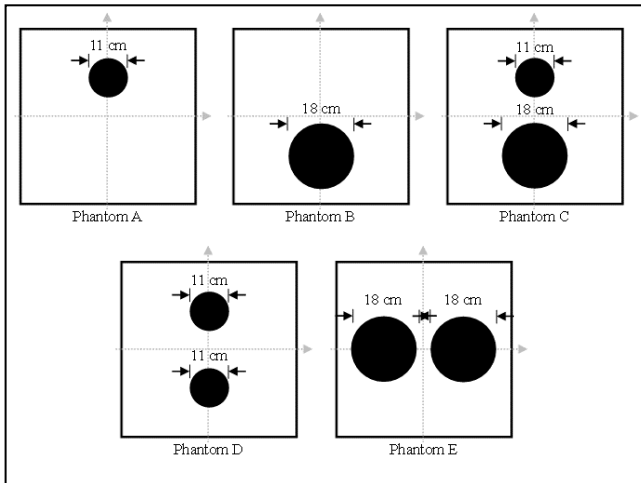


Figure 4 Experimental design of rice moisture phantoms

2.2 Data Acquisition Technique

In designing a tomography system, the accuracy and stability of the sensory structure are determined primarily by the data acquisition technique. In this RTI system, the WSN's layout architecture is based on the Basic Service Set (BSS) for Wi-Fi network topology, which entitled each sensor node to exchange data by sharing one gateway [33]. The wireless peer-to-peer network communication involved 20 RF sensor nodes, signified by the Wi-Fi module ESP8266, with an operating frequency of 2.4 GHz. The RF sensor nodes are configured to perform dual functions (transceiver): enabling them to transmit and receive the RF signals (RSS value). This sensory system constructed a sequential excitation and measurement procedure before entering the signal processing unit. Figure 5 illustrates the block diagram of the RTI network communication system. According to the block diagram, the RTI data acquisition system consists of an access point (Wi-Fi router), 20 RF sensor nodes (ESP8266), a cloud-hosted (Firebase) and a personal computer.

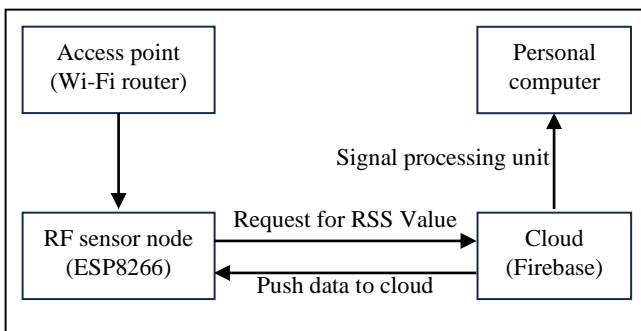


Figure 5 Block diagram of the RTI network communication system

In order to activate the system's network communication, all RF sensor nodes are initially configured to connect to the access point. Simultaneously, the cloud-hosted, Firebase platform is launched to request the RSS reading from the RF sensor node, N1. This sensor node, N1, would perform as the receiver and communicate consecutively with the remaining sensor nodes (N2 to N20) to transmit the RF signals. Then, the measured RSS value at the N1 receiver would be sent to the Firebase through Message Queue Telemetry Transport (MQTT) protocol. The Firebase is an online platform that allows users to store and synchronise data in real-time using a cloud-hosted, NoSQL database. The measurement system would automatically receive RSS data until the sensor node, N20, finished transmitting data to the Firebase and disconnected as the receiver.

2.3 Image Reconstruction Technique

The tomographic images are generally derived by solving the forward and inverse problems. Firstly, a forward problem is addressed to estimate the theoretical scattered electromagnetic field measurements calculated at each excited RF sensor node. Then, an inverse problem is solved to acquire the tomogram of the rice silo cross-section using both linear and non-linear image reconstruction algorithms.

2.3.1 Solving Forward Problem

As aforementioned, the experimental work utilised RF transmission links within the WSN monitoring area to assess the RSS attenuation values. When an RF signal propagates in line-of-sight (LOS) from a transmitter through a medium, the power received at the respective receiver deteriorates as it covers a distance or crosses an attenuating object, which reduces the signal's strength. In an RTI network, this phenomenon is generally defined as link shadowing loss, as illustrated in Figure 6 [24].

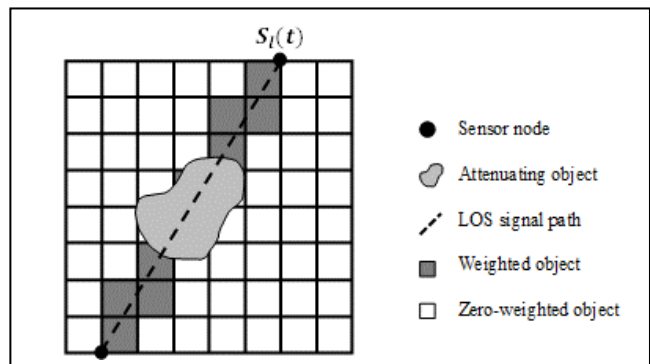


Figure 6 An example of a link in an RTI network that travels in a direct LOS path

The voxel grid is assigned as an element when referring to the actual 3D space, which is analogous to a pixel in 2D space. Since the weighted voxels

(darkened) representing the signal attenuation are known, the shadowing loss, $S_l(t)$ can be estimated as in Equation (2) [34].

$$S_l(t) = \sum_{j=1}^N w_{lj} x_j(t) \quad (2)$$

Where w_{lj} is the weighting of voxel j for link l and $x_j(t)$ is the attenuation level in a voxel j at a certain time, t . Therefore, Equation 3 is applied to express the coexisting RSS value changes, y for each transmission link in the RTI network area.

$$y = Wx + \Delta n \quad (3)$$

Where y is the vector of the measured RSS, W is the $n \times m$ weighting matrix, x is the expected attenuation image, which has to be determined and Δn is the noise vector.

In this study, the RSS measurement is recorded in two conditions. Firstly, when the RTI system is calibrated without rice moisture phantoms, and secondly, when the phantoms are placed inside the silo. Thus, by utilising the RTI-based approach, assessing the difference between the two RSS readings can lead to the localisation of the rice moisture phantom.

2.3.2 Solving Inverse Problem

Measurement data collected from the tomography sensory system can be acquired through various techniques. However, an appropriately chosen image reconstruction algorithm is essential in generating a quality cross-sectional image for a tomography system. In this study, three types of image reconstruction algorithms are employed, which are linear algorithm, iterative algorithm, and non-linear algorithm.

The most popular linear algorithms applied in the tomography system are Linear Back Projection (LBP) and Filtered Back Projection (FBP) algorithms [35]. In the LBP algorithm, a linear image mapping is reconstructed by adding all the cross-products of the projection data from each sensor node with its corresponding sensor loss value [36]. The LBP algorithm is widely recognised for its straightforward and fast reconstruction technique. While for the FBP algorithm, a filter matrix is introduced to sharpen the generated image obtained through the LBP technique. This technique has suppressed the blurring effect produced by the LBP algorithm but also enhances the image noises [37]. Equations (4) and (5) describe the mathematical equations for the LBP and FBP algorithms.

$$G_{LBP}(x'y) = \sum_{j=1}^{20} \sum_{i=1}^{20} L_{ji} \times \bar{J}_{ji}(x'y) \quad (4)$$

$$\text{Where } L_{ji} = S_{ji}^{tot} - S_{ji}^{inc} \text{ and } \bar{J}_{ji} = \frac{J_{ji}}{W}$$

W is the summation of total sensitivity maps, also known as the weight-balanced matrix (WBM), while L_{ji} is the sensor loss. S_{ji}^{tot} is defined by the electric field measured when there is a rice moisture phantom with 'X' MC inside the monitoring area, and S_{ji}^{inc} is the electric field measured before the presence of the phantom.

$$G_{FBP}(x'y) = F(x'y) \times G_{LBP}(x'y) \quad (5)$$

$$\text{Where } F = \frac{P_m}{W}$$

Where P_m is the maximum pixel magnitude in the weight-balanced matrix, W .

Newton's One-step Error Reconstruction (NOSER) algorithm is an example of the iterative algorithm [38]. While soft-field tomography delivers more advantages to be applied in their inhomogeneous experimental setup, these researchers have to face the drawbacks of a long and complex computation process. Therefore, they proposed that the forward problem only needs to be solved once instead of solving the forward problem at every different conductivity distribution. By applying the NOSER algorithm and solving the second iterative step through measurement from sensor nodes at the reference distribution model, [38] have successfully presented a better algorithm performance by reducing systematic errors and increasing the image reconstruction stability. Equation (6) displays the NOSER algorithm formulation.

$$G_{NOSER}(x'y) = [H]^T \times \sum_{j=1}^{20} \sum_{i=1}^{20} LS_{ji} \times \bar{J}_{ji}(x'y) \quad (6)$$

$$\text{Where } LS_{ji} = [S_{ji}^{tot} - S_{ji}^{inc}]^2$$

$$\text{and } H = J_{ji}(x'y) * [J_{ji}(x'y)]^T$$

LS_{ji} is calculated using the least square method. The least-square method minimises the variation between the S_{ji}^{tot} and S_{ji}^{inc} for a given electric field distribution in the computational domain [39]. H is the Hessian matrix that acts as the stabiliser, and $J_{ji}(x, y)$ is the computed Jacobian matrix described above. In addition, the transposed Hessian matrix is utilised as a rough approximation instead of an inverse matrix because it is impossible to compute the direct inverse [40].

The ill-posed inverse problem in the essence of soft-field tomography is making the measurement data highly sensitive to noise. Based on the literature study, the most conventional non-linear algorithm utilised to solve this problem is Tikhonov Regularisation (TR) [41]. The additional regularisation parameter introduced to the mathematical model has minimised the noise spikes through the TR algorithm, which later smoothed the reconstructed image [42]. Furthermore, since this parameter can be predetermined, real-time image processing with acceptable imaging results is possible [27, 41]. Equation (7) represents the mathematical formulation of the TR algorithm employed to reconstruct the rice moisture phantoms [28].

$$G_{\text{tikh}}(x', y) = U \times V \times \text{diag}(T_{\text{tikh}, \kappa}) \times \sum_{j=1}^{20} \sum_{i=1}^{20} LS_{ji} \times \bar{J}_{ji}(x', y) \quad (7)$$

Where $T_{\text{tikh}, \kappa} = \frac{\rho}{\rho^2 + \kappa}$
and $\rho = \text{diag}(\Sigma)$

U and V are unitary matrices, and Σ is a diagonal matrix. The diagonal elements of Σ are singular values, ρ . Based on the equations above, the involved regularisation would introduce additional information into the mathematical model to handle these small singular values, consequently stabilising the inverse problem [43]. Tikhonov's smoothing approach is influenced by this regularisation parameter, κ , where $\kappa > 0$. Based on the initial analysis, the value of the MSSIM index for $\kappa = 1 \times 10^{19}$ and $\kappa = 1 \times 10^{20}$ was calculated and similarly found at 0.3928. The iteration is therefore concluded to have reached its limitation when a constant value of the image quality assessment is recorded [28]. Thus, the same κ value is chosen as the optimum regularisation parameter to construct the phantoms' profiles.

2.4 Image Thresholding Technique

In tomographic images, the quality of an image for post-processing analysis could be improved by introducing a thresholding technique [44]. In this study, the thresholding technique is an approach to segment the rice moisture phantom from the background region by removing unwanted noises, thus, transforming the reconstructed images into a presentable state for more straightforward image analysis. This technique involves choosing a threshold ratio, T , which is the ratio of a pixel value relative to the maximum pixel value. Any pixel value lower than the preferred threshold ratio defined by T would be rounded to zero. The approach, known as a global thresholding technique, is presented in Equation (8).

$$G_T(x, y) = \begin{cases} G(x, y), & G(x, y) \geq T \\ 0, & G(x, y) < 0 \end{cases} \quad (8)$$

However, specifying a standard threshold ratio that can be used for all tested phantoms is crucial. To ensure the technique is reasonable, all reconstructed images obtained from LBP, FBP, NOSER and TR algorithms experienced the same global thresholding process. The threshold ratio is firstly assessed by testing the total 60 reconstructed images with all possible thresholding values ranging from 0.01 to 1.00 (100 steps). Then, the best threshold ratio is selected based on the maximum score exhibited by the image quality indexes, the Mean Structural Similarity Index (MSSIM) [23]. Finally, the median value from the best threshold ratio is calculated and chosen as the standard thresholding value respecting each image reconstruction algorithm LBP, FBP, NOSER and TR. The median value is selected since it is less affected by the outliers' data, which, therefore, is practical for comparing the different rice moisture phantoms [45].

An offline global thresholding analysis is performed to acquire the best threshold values based on the highest image quality indexes, MSSIM, concerning the reference images. Figure 7 describes an example of the applied thresholding steps in the experimental study of rice moisture phantoms obtained by the LBP algorithm at a 15% percentage of MC. Meanwhile, based on the LBP algorithm, Table 1 tabulates the calculated median value among the best threshold ratios for rice moisture phantoms at 15%, 20% and 25% MC.

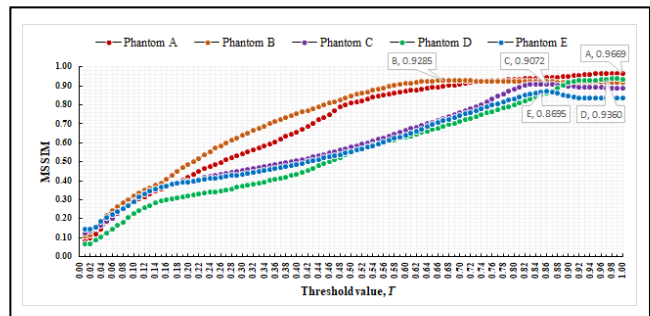


Figure 7 Example of thresholding step on phantoms' profiles A, B, C, D and E at 15% moisture content using LBP algorithm

Table 1 The best threshold ratio for rice moisture phantoms obtained by the LBP algorithm

Phantom	Percentage of Moisture Content		
	15%	20%	25%
A	1.00	1.00	0.96
B	0.67	1.00	0.97
C	0.86	0.88	0.86
D	0.97	0.93	0.95
E	0.85	0.91	0.90
Median	0.86	0.93	0.95

Table 2 below summarises the global threshold ratio selected based on the unbiased median probability through the maximum score exhibited by the MSSIM index for all image reconstruction algorithms LBP, FBP, NOSER and TR. Since each algorithm produced different baselines for the maximum pixel value in the reconstructed images, the thresholding results are quantified concerning each respective algorithm.

Table 2 Median threshold ratio by different image reconstruction algorithms

Algorithm	Percentage of Moisture Content		
	15%	20%	25%
LBP	0.86	0.93	0.95
FBP	0.97	1.00	1.00
NS	0.85	0.87	0.86
TR	0.92	0.93	0.93

3.0 RESULTS AND DISCUSSIONS

This section discusses and analyses the outcomes of the experimental study following the methodologies detailed in the previous section. The effectiveness of the proposed RTI system is validated by using the selected image reconstruction algorithms to image the rice moisture phantoms. Furthermore, numerical analysis is also conducted using linear regression models to evaluate the efficiency of the rice moisture sensing system in each case study.

3.1 Image Assessment Analysis

Tables 3, 4, 5 and 6 describe the five phantoms' profiles utilising LBP, FBP, NOSER and TR algorithms, respectively. Every reconstructed and thresholded image is compared with its corresponding reference image. Generally, all four image reconstruction algorithms have adequately generated images corresponding to the reference images for all percentages of 15%, 20% and 25% MC.

Based on the reconstructed images, it is evident that the spot with higher colour intensity is concentrated in the targeted location, indicating the

distribution of the rice moisture phantoms. However, these results also illustrated that, as the number and size of the rice moisture phantoms increased, the background artefacts gradually marked up the imaging results, which, unfortunately, enhanced the noise background. These scenarios are depicted mostly by the LBP and FBP algorithms compared to the NOSER and TR algorithms because the back-projection techniques used by the LBP and FBP algorithms often result in artefacts that reduce the accuracy [42].

On the other hand, the NOSER and TR algorithms have visually generated good tomogram images by minimising the noise floor artefacts due to their non-linear approach to solving the inverse problem.

The following application of the simple thresholding technique has effectively removed the background artefacts in the reconstructed images, thus illustrating the imaging results in uncluttered tomograms. However, it can also be noticed that the pre-set global threshold values have been producing over-thresholded images, where only several rice moisture phantoms have good thresholded images.

The previous discussion regarding the imaging results is briefly based on human eye tolerance, and this method is called the subjective method. Hence, to investigate the method's feasibility, the performance of the executed tomograms is evaluated using image quality assessment concerning the reference MC distribution.

In tomographic imaging, the image quality assessment is an essential benchmark for evaluating the reconstructed image quality. In this study, the MSSIM index has been employed to quantify the reconstructed images. The recorded parameter compares the structural similarity between two images and generates an index ranging from zero to one (0-1). Higher values of the MSSIM index indicate that the reconstructed image is likely identical to the reference image. The evaluated image is indexed based on structure, luminance, and contrast [46, 47]. The overall results of the MSSIM index for rice moisture phantoms A, B, C, D and E at 15%, 20%, and 25% MC are tabulated in Tables 7 and 8.

Table 3 Reconstructed and thresholded images of rice moisture phantoms using the LBP algorithm


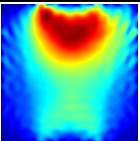
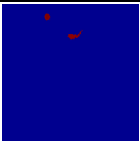
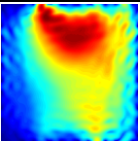
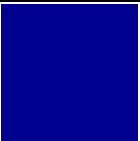
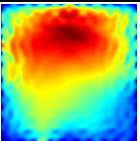
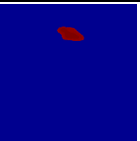

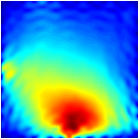
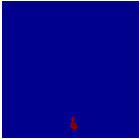
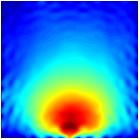
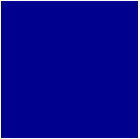
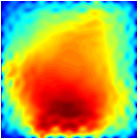
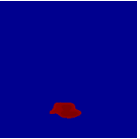

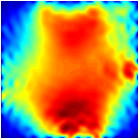
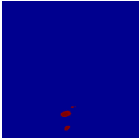
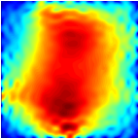

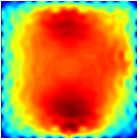
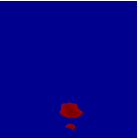

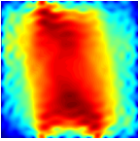
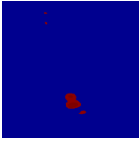
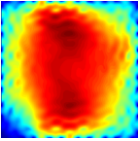

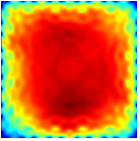
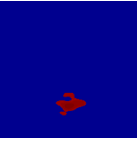

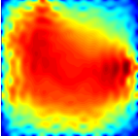
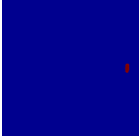
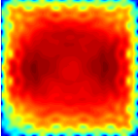

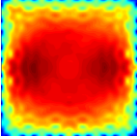
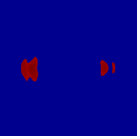
Phantom	15% MC		20% MC		25% MC	
	Reconstructed	Thresholded	Reconstructed	Thresholded	Reconstructed	Thresholded
 A						
 B						
 C						
 D						
 E						

Table 4 Reconstructed and thresholded images of rice moisture phantoms using the FBP algorithm


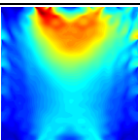
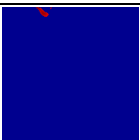
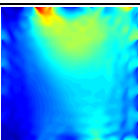
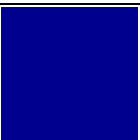
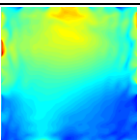


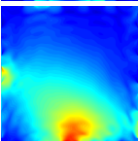
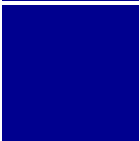
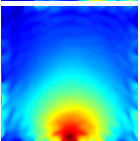
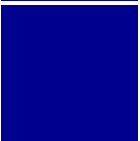
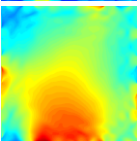


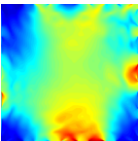
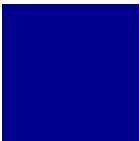
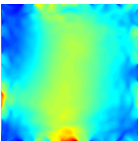
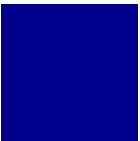
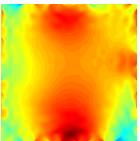
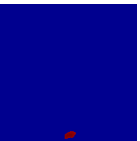

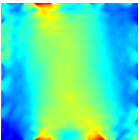
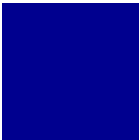
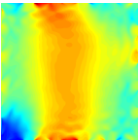
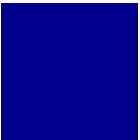
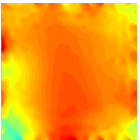


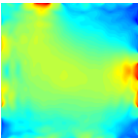
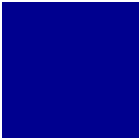
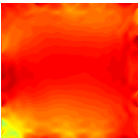
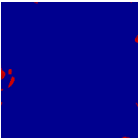
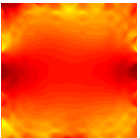

Phantom	15% MC		20% MC		25% MC	
	Reconstructed	Thresholded	Reconstructed	Thresholded	Reconstructed	Thresholded
 A						
 B						
 C						
 D						
 E						

Table 5 Reconstructed and thresholded images of rice moisture phantoms using the NOSER algorithm

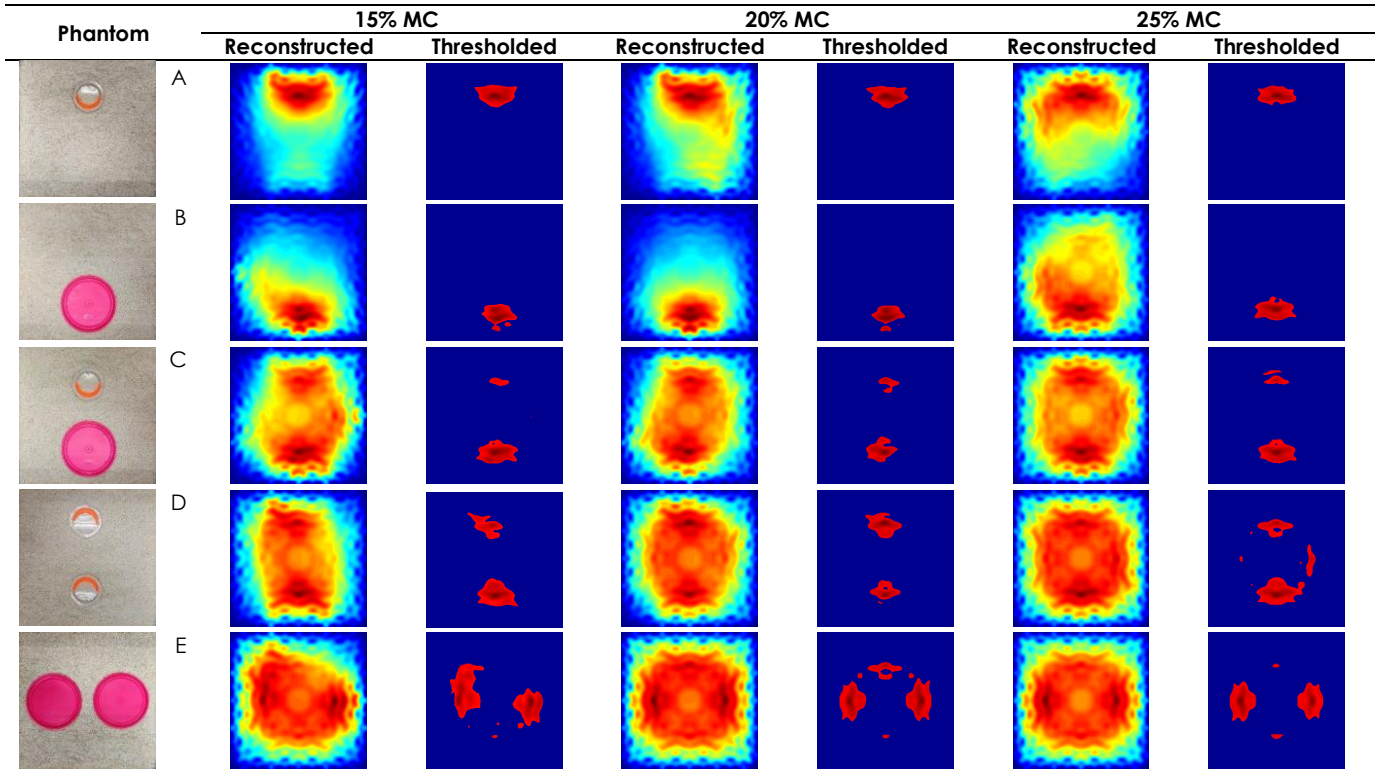


Table 6 Reconstructed and thresholded images of rice moisture phantoms using the TR algorithm

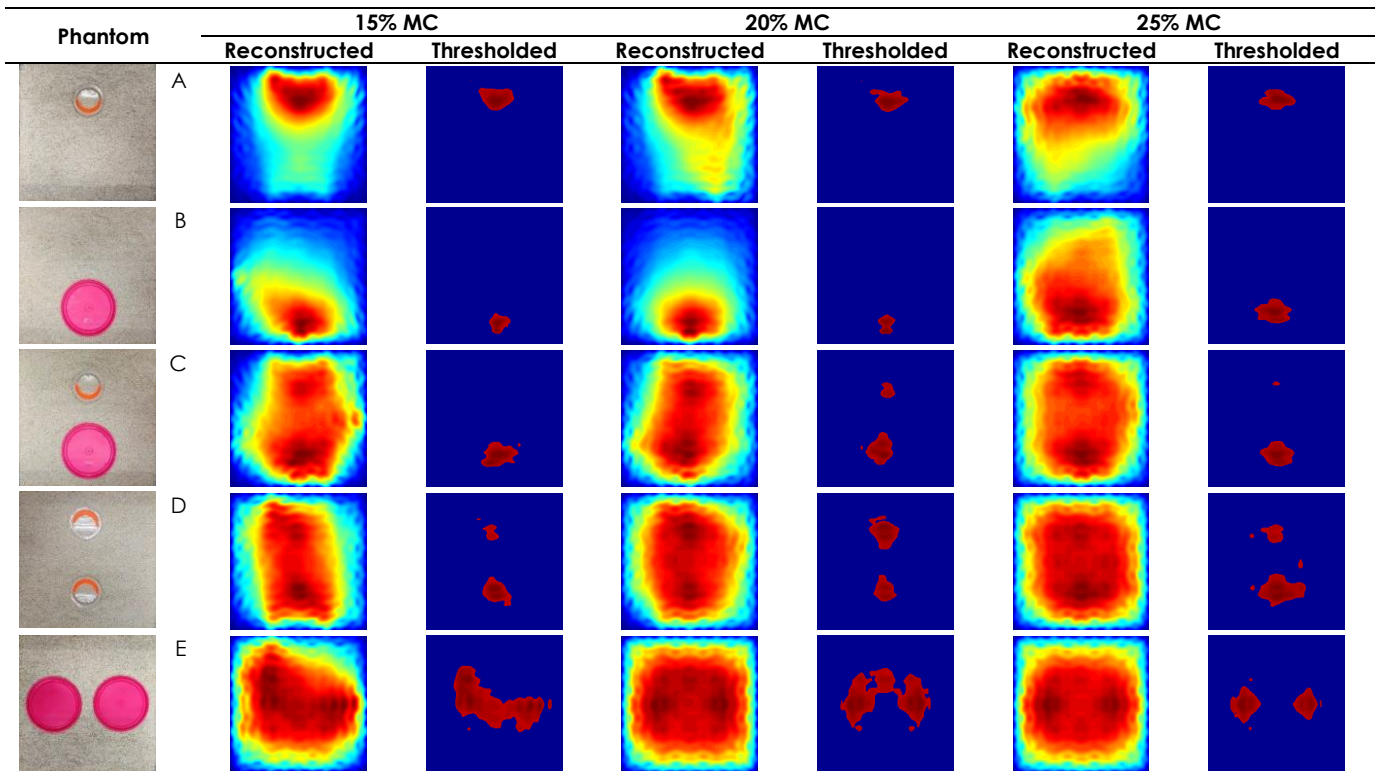


Table 7 MSSIM indexes measured on the reconstructed image of rice moisture phantoms

Phantom	15% MC				20% MC				25% MC			
	LBP	FBP	NS	TR	LBP	FBP	NS	TR	LBP	FBP	NS	TR
A	0.2942	0.2830	0.3261	0.3075	0.2914	0.2808	0.3191	0.3027	0.2875	0.2782	0.3109	0.2968
B	0.3301	0.3136	0.3566	0.3424	0.3267	0.3119	0.3557	0.3405	0.3288	0.3176	0.3496	0.3378
C	0.3541	0.3365	0.3773	0.3649	0.3516	0.3318	0.3718	0.3605	0.3506	0.3412	0.3688	0.3589
D	0.3104	0.2967	0.3330	0.3198	0.3096	0.2994	0.3312	0.3185	0.3080	0.2993	0.3277	0.3160
E	0.3918	0.3665	0.4087	0.4002	0.3924	0.3843	0.4067	0.3994	0.3925	0.3843	0.4070	0.3997

Table 8 MSSIM indexes measured on the thresholded image of rice moisture phantoms

Phantom	15% MC				20% MC				25% MC			
	LBP	FBP	NS	TR	LBP	FBP	NS	TR	LBP	FBP	NS	TR
A	0.9658	0.9678	0.9715	0.9734	0.9678	0.9674	0.9734	0.9733	0.9738	0.9653	0.9726	0.9785
B	0.9179	0.9091	0.9304	0.9252	0.9191	0.9191	0.9174	0.9132	0.9226	0.9191	0.9293	0.9325
C	0.8866	0.8871	0.9079	0.9053	0.8871	0.8867	0.9021	0.9090	0.8925	0.8871	0.9074	0.9055
D	0.9377	0.9354	0.9469	0.9503	0.9360	0.9347	0.9542	0.9589	0.9420	0.9354	0.9350	0.9447
E	0.8369	0.8380	0.8699	0.8726	0.8385	0.8383	0.8612	0.8704	0.8485	0.8383	0.8745	0.8727

Tables 7 and 8 display the image quality assessment, MSSIM, assessed from the overall image reconstruction algorithms for the experimental study of rice moisture phantoms. Based on the results, each image reconstruction algorithm delivered acceptable MSSIM values at all percentage of rice MC levels (15%, 20%, and 25%).

Before the thresholding process, the maximum and minimum scores for the MSSIM index are 0.4087 at 15% MC of Phantom E using the NOSER algorithm and 0.2782 at 25% MC of Phantom A using the FBP algorithm, respectively. Throughout the percentage of MC studies, the NOSER algorithm consistently had the highest MSSIM indexes, outperforming all other algorithms. On the contrary, the FBP algorithm normally produced the lowest MSSIM values.

The NOSER algorithm remarkably shows exceptional performance feasibly due to its iterative approach involving measurements from sensor nodes within the reference distribution model [38]. Regarding the contradictory MSSIM results acquired by the FBP algorithm, previous analysis [37] believed that the filter matrix in the FBP algorithm leads to the amplification of the image noise, resulting in imprecise image reconstruction results.

Based on Table 8, the thresholded imaging results, as expected, improved the overall image quality values for all rice moisture levels (15%, 20% and 25%). The maximum score of the MSSIM index is 0.9785 at 25% moisture content of Profile A using the TR algorithm, while the minimum score of the MSSIM index is 0.8369 at 15% moisture content of Profile E using the LBP algorithm.

Although the thresholded results have eliminated the unwanted artefacts, several phantoms' profiles have been over-thresholding. Besides, regarding the image reconstruction algorithms, it can be observed that the thresholded images inconsistently represent which algorithm is the best for rice moisture imaging at every percentage of MC. These issues are mainly due

to the approach of global thresholding that considers the threshold value by concerning the overall rice moisture phantoms while constituting the highest image quality score from the MSSIM assessment [48].

According to Table 3, the FBP algorithm clearly described an ineffective result of the thresholding technique. Most of the thresholded phantoms are disappeared due to over-threshold conditions. Corresponding to the finding by reference [35], the dot product between the filter and LBP matrices has shifted the colour scale on the reconstructed image when the FBP algorithm is applied in the soft-field tomography. Therefore, the subsequent global thresholding technique has generated these underperformance results. Nevertheless, as discussed in the previous section, the thresholding technique was purposely adopted to enhance the reconstructed images into a presentable and direct state.

In this study, the thresholding technique has been proven to be the solution for eliminating back-projection artefacts. With artefacts being removed, the errors resulting from the artefacts are also reduced. However, integrating a more sophisticated thresholding technique, such as Otsu and adaptive thresholding technique [49, 50, 51], could solve the problem of over-thresholded images and improve the thresholding effectiveness.

3.2 Maximum Pixel Value Analysis

Generally, the higher pixel intensity in the reconstructed RTI images signifies the estimated phantoms' location, shape, and size. By emphasising the variations in colour scale, the reconstructed RTI images have successfully identified the existence of the rice moisture phantoms. Nevertheless, these tomograms only produced reliable information for the location and size of the moisture distribution. Due to the smearing effects, it is also challenging to differentiate the changes in the percentage of MC.

Accordingly, a measurable quantitative analysis is at least necessitated.

In this study, an individual pixel of the reconstructed tomogram has produced its certain intensity based on the scattered electric field, which is approximated by the contrasting permittivity distribution. Hence, the maximum weighting pixel of the reconstructed images should indicate its relative percentage of MC. Based on this understanding, the maximum pixel value from the reconstructed RTI image's grid can be utilised to form a simple linear regression plot. This subsection intends to investigate the correlation between different percentages of MC and the maximum pixel values based on the linear regression plot and examine the feasibility of the developed approach for a percentage of rice moisture approximation. The linear regression model is applied to estimate the value of the dependent variable (maximum pixel value) at a definite value of the independent variable (percentage of MC).

Since the image reconstruction algorithms delivered different baselines of the maximum pixel values, the data is quantified using the percentage ratio over the maximum pixel value acquired from the tomogram of the reference medium, where the rice moisture phantom is absent. Then, based on the calculation, the maximum pixel value in terms of percentage for all algorithms can be appropriately evaluated.

Figure 8 displays the linear regression model of the percentage of maximum pixel value as a function of moisture content by employing LBP, FBP, NOSER and TR algorithms. The scattered data plot establishes a linear fitting line for all image reconstruction algorithms concerning each phantom's profile. All four algorithms have conclusively identified a positive correlation between the percentage of MC and the maximum pixel value. A positive correlation indicates that the maximum pixel value increases as the percentage of MC increases.

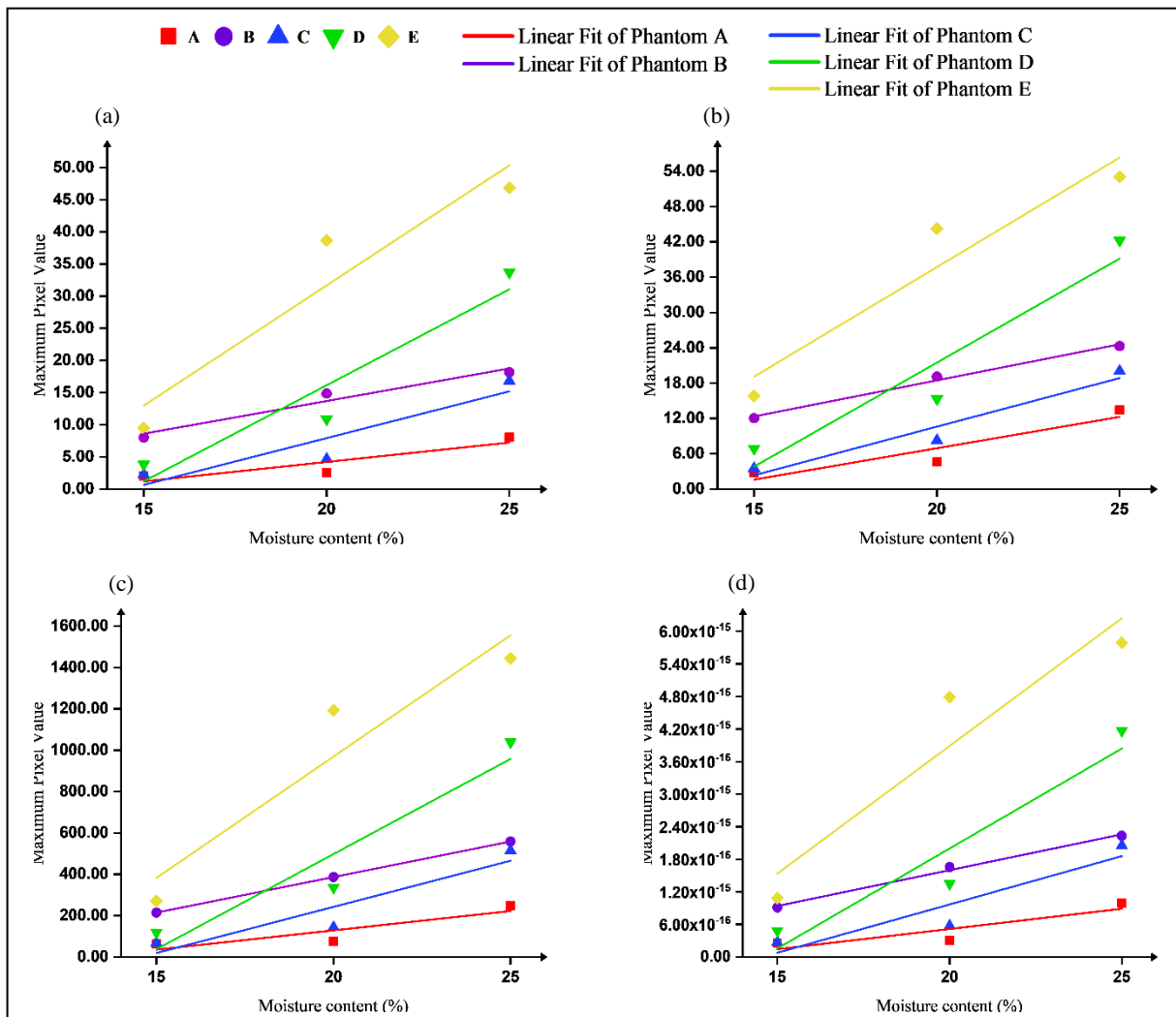


Figure 8 Percentage of maximum pixel value using (a) LBP (b) FBP (c) NOSER and (d) TR algorithms

3.2.1 Linear Regression Model

The positive correlation between the percentage of MC and the maximum pixel value can be quantitatively analysed using a linear regression model. Since the maximum pixel value linearly increased with the percentage of MC, a first-order polynomial regression model is preliminarily predicted, as shown in Equation (8) [52].

$$PV_{max} = aMC + b \quad (8)$$

Where a and b are the specific notations of the regression model based on the rice moisture phantoms. Besides, the a is also defined as the regression coefficient representing the gradient of the fitted line [52], by which the number of maximum pixel values positively changed on average as the percentage of MC increased by one unit.

Besides, in order to indicate the strength of the linear relationship between the percentage of rice MC and the maximum pixel value, the correlation coefficient, R^2 is analysed. The R^2 value ranges from 0 to 1 and is generally interpreted as the statistical value determining how close the plotted data are to the fitted regression line [53]. A higher R^2 value describes

that the variation in the dependent variable (maximum pixel value) strongly correlates with the independent variable (percentage of MC).

Table 9 describes the statistical linear regression analyses performed in the experimental study through LBP, FBP, NOSER and TR algorithms. Based on the corresponding table, all rice moisture phantoms indicate that the number of the maximum pixel value is significantly influenced by the percentage of rice MC, with the lowest correlation coefficient, R^2 , of 0.8051 for Profile A using the NOSER algorithm. Meanwhile, the highest recorded correlation coefficient, R^2 , is 0.9988 for Profile B, also using the NOSER algorithm. As reflected by a higher R^2 value, these results consequently supported that the variation in the maximum pixel value strongly correlates with the percentage of moisture content, regardless of the location and size of the rice moisture phantoms.

Table 9 also deduced that all image reconstruction algorithms consistently express the highest regression coefficient, a , on rice Phantom E, followed by D, C, B and Phantom A. These results demonstrated that, at a similar size of the monitored area, the bigger the moisture distribution, the more significant the percentage of MC shifting can affect the number of the maximum pixel value.

Table 9 Correlation coefficients of the linear regression model using LBP, FBP, NOSER and TR algorithms

Algorithm	Phantom	Linear Regression Model	Correlation Coefficient, R^2
LBP	A	$PV_{max} = 6.04 \times 10^1 MC - 7.85 \times 10^0$	0.8096
	B	$PV_{max} = 10.10 \times 10^1 MC - 6.60 \times 10^0$	0.9604
	C	$PV_{max} = 14.50 \times 10^1 MC - 21.10 \times 10^0$	0.8691
	D	$PV_{max} = 29.90 \times 10^1 MC - 43.60 \times 10^0$	0.9151
	E	$PV_{max} = 37.40 \times 10^1 MC - 43.00 \times 10^0$	0.9040
FBP	A	$PV_{max} = 10.70 \times 10^1 MC - 14.40 \times 10^0$	0.8746
	B	$PV_{max} = 12.30 \times 10^1 MC - 6.05 \times 10^0$	0.9921
	C	$PV_{max} = 16.50 \times 10^1 MC - 22.40 \times 10^0$	0.9427
	D	$PV_{max} = 35.30 \times 10^1 MC - 49.20 \times 10^0$	0.9169
	E	$PV_{max} = 37.20 \times 10^1 MC - 36.70 \times 10^0$	0.9147
NS	A	$PV_{max} = 1.87 \times 10^3 MC - 2.45 \times 10^2$	0.8051
	B	$PV_{max} = 3.44 \times 10^3 MC - 3.01 \times 10^2$	0.9988
	C	$PV_{max} = 4.47 \times 10^3 MC - 6.51 \times 10^2$	0.8718
	D	$PV_{max} = 9.21 \times 10^3 MC - 13.40 \times 10^2$	0.9452
	E	$PV_{max} = 11.70 \times 10^3 MC - 13.80 \times 10^2$	0.9013
TR	A	$PV_{max} = 7.46 \times 10^{-15} MC - 1.32 \times 10^{-16}$	0.8077
	B	$PV_{max} = 13.20 \times 10^{-15} MC - 11.10 \times 10^{-16}$	0.9945
	C	$PV_{max} = 17.80 \times 10^{-15} MC - 10.90 \times 10^{-16}$	0.8720
	D	$PV_{max} = 36.90 \times 10^{-15} MC - 12.60 \times 10^{-16}$	0.9143
	E	$PV_{max} = 47.10 \times 10^{-15} MC - 10.10 \times 10^{-16}$	0.9010

4.0 CONCLUSION

A radio tomographic imaging system for localization towards rice moisture content distribution sensing has been successfully designed and developed, and the investigation on the efficiency and accuracy of the system's performance was executed. In conclusion, the experimental study has effectively demonstrated that the RTI system can locate and monitor the rice moisture distribution with acceptable precision through all four image algorithms.

It can be primarily deduced that as the number and size of the rice moisture phantoms increased, the smearing artefacts gradually marked up the reconstructed tomogram images. Furthermore, from the overall phantoms' profiles, it is concluded that NOSER and TR algorithms deliver more accurate imaging results compared to LBP and FBP algorithms. The consecutive application of the global thresholding technique has eliminated the background artefacts. However, there is a weakness in the thresholding approach as it can be noticed that the pre-set global threshold values have been producing over-thresholded images, where only specific phantoms' profiles have good outcomes. Last but not least, the implemented numerical analysis, which constantly delivered higher R^2 values, has supported the possibility of employing the maximum pixel value of the RTI images for monitoring the percentage of rice MC, regardless of the location and size of the rice phantoms.

The popularity of RTI implementation is mainly due to its accessibility and cost-effectiveness. Since deploying RF sensor nodes is relatively simple and inexpensive, a larger and more flexible sensing area is adaptable compared to other approaches that may be unfeasible. Besides, the remarkable approach of this technique is that it allows repeatable measurements on the same material over a duration of time, which could be applied to monitor several material properties corresponding with the control system as desired. Last but not least, the non-destructive approach using a numerical analysis that can determine the percentage of MC based on the reconstructed RTI images would sustainably preserve the volume of the rice grains throughout the storage operation.

Conflicts of Interest

The authors declare that there is no conflict of interest regarding the publication of this paper.

Acknowledgement

The authors would like to thank Ministry of Higher Education (MOHE) Malaysia for funding this research under the Transdisciplinary Research Grant Scheme (Ref: TRGS/1/2018/UNIMAP/02/4/2). Special

acknowledgement also goes to Universiti Malaysia Perlis for providing the facilities and technical support.

References

- [1] Kumar, S. and K. Prasad. 2018. Effect of Parboiling and Puffing Processes on the Physicochemical, Functional, Optical, Pasting, Thermal, Textural and Structural Properties of Selected Indica Rice. *Journal of Food Measurement and Characterization*. 12(3): 1707-1722.
- [2] You, K. Y., L. L. You, C. S. Yue, K. Mun, C. S. Yue, H. K. Mun and C. Y. Lee. 2017. Physical and Chemical Characterization of Rice using Microwave and Laboratory Methods. In *Rice - Technol. Prod., Amanullah, S. Fahad*, eds. 1st ed. InTech. 81-99.
- [3] Müller, A., M. T. Nunes, V. Maldaner, P. C. Coradi, R. S. de Moraes, S. Martens, A. F. Leal, V. F. Pereira and C. K. Marin. 2022. Rice Drying, Storage and Processing: Effects of Post-harvest Operations on Grain Quality. *Rice Science*. 29(1): 16-30.
- [4] Alhendi, A. S., S. H. Al-Rawi and A. M. Jasim. 2019. Effect of Moisture Content of Two Paddy Varieties on the Physical and Cooked Properties of Produced Rice. *Brazilian Journal of Food Technology*. 22.
- [5] Naik, D. S. and M. B. Chetti. 2017. Influence of Packaging and Storage Conditions on the Moisture Content and Its Effect on Fungal Load of Paddy. *Research Journal of Agricultural Sciences*. 8(2): 370-374.
- [6] Shafiekhani, S., S. A. Wilson and G. G. Atungulu. 2018. Impacts of Storage Temperature and Rice Moisture Content on Color Characteristics of Rice from Fields with Different Disease Management Practices. *Journal of Stored Products Research*. 78: 89-97.
- [7] Putri, R. E., A. Yahya, N. M. Adam and S. A. Aziz. 2015. Related Fracture Resistance with Moisture Content in Different Grain Orientation of Paddy Grain. *Journal of Biology, Agriculture and Healthcare*. 11: 64-70.
- [8] Nelson, S. O. and S. Trabelsi. 2012. A Century of Grain and Seed Moisture Measurement by Sensing Electrical Properties. *Transactions of the ASABE*. 55(2): 629-636.
- [9] Edwards, K., N. Geddert, K. Krakalovich, R. Kruk, M. Asefi, J. Lovetri, C. Gilmore and I. Jeffrey. 2020. Stored Grain Inventory Management using Neural-network-based Parametric Electromagnetic Inversion. *IEEE Access*. 8: 207182-207192.
- [10] Nelson, S. O. 2015. Chapter 13 - Dielectric properties Models for Grain and Seed Dielectr. *Prop. Agric. Mater. Their Appl.* Academic Press, ed. Elsevier Inc. 175-193.
- [11] Mazima, J. K., A. Johnson, E. Manasseh and S. Kajjage. 2018. An Overview of Electromagnetic Radiation in Grain Crops. *International Journal of Food Science and Technology*. 1(1): 21-32.
- [12] Nelson, S. O. 2015. Chapter 15 - Dielectric Properties Data. Elsevier Inc.
- [13] Nath K, D. and P. Ramanathan. 2017. Non-destructive Methods for the Measurement of Moisture Contents - A Review. *Sensor Review*. 37(1): 71-77.
- [14] Brisard, S., M. Serdar and P. J. M. Monteiro. 2020. Multiscale X-ray Tomography of Cementitious Materials: A Review. *Cement and Concrete Research*. 128(November 2019).
- [15] Tang, C. S., C. Zhu, T. Leng, B. Shi, Q. Cheng and H. Zeng. 2019. Three-dimensional Characterization of Desiccation Cracking Behavior of Compacted Clayey Soil using X-Ray Computed Tomography. *Engineering Geology*. 255(December 2018): 1-10.
- [16] Couceiro, J., O. Lindgren, L. Hansson, O. Söderström and D. Sandberg. 2019. Real-time Wood Moisture-content Determination using Dual-energy X-ray Computed Tomography Scanning. *Wood Material Science and Engineering*. 14(6): 437-444.

- [17] Rymarczyk, T., J. Sikora and P. Tchórzewski. 2018. Implementation of Electrical Impedance Tomography for Analysis of Building Moisture Conditions. *COMPEL - The International Journal for Computation and Mathematics in Electrical and Electronic Engineering*. 37(5): 1837-1861.
- [18] Jong, S. M. de, R. A. Heijnen, W. Nijland and M. van der Meijde. 2020. Monitoring Soil Moisture Dynamics using Electrical Resistivity Tomography under Homogeneous Field Conditions. *Sensors (Switzerland)*. 20(18): 1-18.
- [19] Martin, L., H. Cocharad, S. Mayr and E. Badel. 2021. Using Electrical Resistivity Tomography to Detect Wetwood and Estimate Moisture Content in Silver Fir (*Abies alba* Mill.). *Annals of Forest Science*. 78(3).
- [20] Rahman, N. A. A., L. E. Hong, R. A. Rahim, H. A. Rahim, N. Ahmad, S. Bunyamin, K. H. Abas, N. M. N. Ayob, F. R. M. Yunus and M. S. B. Mansor. 2015. A Review: Tomography Systems in Medical and Industrial Processes. *Jurnal Teknologi*. 73(6): 1-11.
- [21] Yao, J. and M. Takei. 2017. Application of Process Tomography to Multiphase Flow Measurement in Industrial and Biomedical Fields: A Review. *IEEE Sensors Journal*. 17(24): 8196-8205.
- [22] Mohd Ramli, N. A., M. H. Fazalul Rahiman, L. M. Kamarudin, L. Mohamed, A. Zakaria, A. Ahmad and R. A. Rahim. 2021. A New Method of Rice Moisture Content Determination using Voxel Weighting-based from Radio Tomography Images. *Sensors (Basel, Switzerland)*. 21(11).
- [23] Rahiman, M. H. F. 2013. Ultrasonic Tomography System for Liquid / Gas Bubble Column. Universiti Teknologi Malaysia.
- [24] Wilson, J. and N. Patwari. 2010. Radio Tomographic Imaging with Wireless Networks. *IEEE Transactions on Mobile Computing*. 9(5): 621-632.
- [25] Erunkulu, O. O., A. M. Zungeru, C. K. Lebekwe and J. M. Chuma. 2020. Cellular Communications Coverage Prediction Techniques: A Survey and Comparison. *IEEE Access*. 8: 113052-113077.
- [26] Obeidat, H., A. Alabdullah, E. Elkhazmi, W. Suhaib, O. Obeidat, M. Alkhambashi, M. Mosleh, N. Ali, Y. Dama, Z. Abidin, R. Abd-Alhameed and P. Excell. 2020. Indoor Environment Propagation Review. *Computer Science Review*. 37: 100272.
- [27] Chiu, C. and D. Dujovne. 2014. Experimental Characterization of Radio Tomographic Imaging using Tikhonov's Regularization. 2014 *IEEE Biennial Congress of Argentina (ARGENCON)*. 468-472.
- [28] Kiat, T. T. W. 2017. Simulation Study of Tomography for Agarwood Evaluation. Universiti Malaysia Perlis.
- [29] Asefi, M., I. Jeffrey, J. LoVetri, C. Gilmore, P. Card and J. Paliwal. 2015. Grain Bin Monitoring via Electromagnetic Imaging. *Computers and Electronics in Agriculture*. 119: 133-141.
- [30] Postharvest Unit, C., 2013. Paddy Drying.
- [31] Azmi, N., L. M. Kamarudin, A. Zakaria, D. L. Ndzi, M. H. F. Rahiman, S. M. M. S. Zakaria and L. Mohamed. 2021. RF-based Moisture Content Determination in Rice using Machine Learning Techniques. *Sensors*. 21(5): 1-20.
- [32] Almaleeh, A. A., A. Zakaria, L. M. Kamarudin, M. H. F. Rahiman, D. L. Ndzi and I. Ismail. 2022. Inline 3D Volumetric Measurement of Moisture Content in Rice using Regression-based ML of RF Tomographic Imaging. *Sensors*. 22(1).
- [33] Kazeem, O. O., O. O. Akintade and L. O. Kehinde. Comparative Study of Communication Interfaces for Sensors and Actuators in the Cloud of Internet of Things. *International Journal of Internet of Things*. 6(1): 9-13.
- [34] Shukri, S. and L. M. Kamarudin. 2017. Device Free Localization Technology for Human Detection and Counting with RF Sensor Networks: A Review. *Journal of Network and Computer Applications*. 97(October 2016): 157-174.
- [35] Wahab, Y. A., R. A. Rahim, M. H. F. Rahiman, S. Ridzuan Aw, F. R. M. Yunus, J. Puspanathan, N. M. N. Ayob, P. L. Leow, H. A. Rahim, I. L. Ahmad, A. Jonet, K. S. Chia and K. S. Tee. 2017. Inverse Problem: Comparison between Linear Back-projection Algorithm and Filtered Back-projection algorithm in Soft-field Tomography. *International Journal of Integrated Engineering*. 9(4): 32-36.
- [36] Goh, C. L., A. R. Ruzairi, F. R. Hafiz and Z. C. Tee. 2017. Ultrasonic Tomography System for Flow Monitoring: A Review. *IEEE Sensors Journal*. 17(17): 5382-5390.
- [37] Schofield, R., L. King, U. Tayal, I. Castellano, J. Stirrup, F. Pontana, J. Earls and E. Nicol. 2020. Image Reconstruction: Part 1 – Understanding Filtered Back Projection, Noise and Image Acquisition. *Journal of Cardiovascular Computed Tomography*. 14(3): 219-225.
- [38] Mallach, M., M. Gevers, P. Gebhardt and T. Musch. 2018. Fast and Precise Soft-field Electromagnetic Tomography Systems for Multiphase Flow Imaging. *Energies* 2018. 11(5): 1-17.
- [39] Mallach, M., P. Gebhardt and T. Musch. 2017. 2D Microwave Tomography System Metal Pipes. *Flow Measurement and Instrumentation*. 53(2017): 80-88.
- [40] Yunus, Y. M., R. A. Rahim, R. G. Green and M. H. F. Rahiman. 2007. Image Reconstruction using Iterative Transpose Algorithm for Optical Tomography. *Jurnal Teknologi*. 47(1): 91-102.
- [41] Cui, Z., Q. Wang, Q. Xue, W. Fan, L. Zhang, Z. Cao, B. Sun, H. Wang and W. Yang. 2016. A Review on Image Reconstruction Algorithms for Electrical Capacitance/Resistance Tomography. *Sensor Review*. 36(4): 429-445.
- [42] Guo, Q., X. Li, B. Hou, G. Mariethoz, M. Ye, W. Yang and Z. Liu. 2020. A Novel Image Reconstruction Strategy for ECT: Combining Two Algorithms with a Graph Cut Method. *IEEE Transactions on Instrumentation and Measurement*. 69(3): 804-814.
- [43] Beck, B., X. Ma and R. Baxley. 2016. Ultrawideband Tomographic Imaging in Uncalibrated Networks. *IEEE Transactions on Wireless Communications*. 15(9): 6474-6486.
- [44] Liedmann, F., C. Holewa and C. Wietfeld. 2018. The Radio Field as a Sensor-A Segmentation based Soil Moisture Sensing Approach. 2018 *IEEE Sensors Applications Symposium, SAS 2018 - Proceedings*. 2018-January: 1-6.
- [45] Mishra, P., C. M. Pandey, U. Singh, A. Gupta, C. Sahu and A. Keshri. 2019. Descriptive Statistics and Normality Tests for Statistical Data. *Annals of Cardiac Anaesthesia*. 22(1): 67-72.
- [46] Wang, Z., A. C. Bovik, H. R. Sheikh and E. P. Simoncelli. 2004. Image Quality Assessment: From Error Visibility to Structural Similarity. *IEEE Transactions on Image Processing*. 13(4): 600-611.
- [47] Banitalebi-Dehkordi, M., M. Khademi, A. Ebrahimi-Moghadam and H. Hadizadeh. 2019. An Image Quality Assessment Algorithm based on Saliency and Sparsity. *Multimedia Tools and Applications*. 78(9): 11507-11526.
- [48] Chang, P. C., K. Liang, J. C. Lim, M. C. Chung and L. Y. Chien. 2013. A Comparison of the Thresholding Strategies of Micro-CT for Periodontal Bone Loss: A Pilot Study. *Dentomaxillofacial Radiology*. 42(2).
- [49] Hoang, N. D 2018. Detection of Surface Crack in Building Structures using Image Processing Technique with an Improved Otsu Method for image Thresholding. *Advances in Civil Engineering*.
- [50] Saddami, K., P. Afrah, V. Mutiawani and F. Arnica. 2019. A New Adaptive Thresholding Technique for Binarizing Ancient Document. 1st 2018 *Indonesian Association for Pattern Recognition International Conference, INAPR 2018 - Proceedings*. 57-61.
- [51] Kurniadi, F. I., D. Septyani and I. S. Pratama. 2020. Local Adaptive Thresholding Techniques for Binarizing Scanned Lampung Aksara Document Images. 2020 3rd *International Conference on Computer and Informatics Engineering, IC2IE 2020*. 135-139.
- [52] Lee, S. W. 2022. Regression Analysis for Continuous Independent Variables in Medical Research: Statistical Standard and Guideline of Life Cycle Committee. *Life Cycle*. 2: 1-8.

- [53] Hope, T. M. H. 2019. Linear Regression. Mach. Learn. Methods Appl. to Brain Disord. Elsevier Inc. 67-81.